

# Efficient numerical method for predicting nonlinear optical spectroscopies of open systems

Peter A. Rose

*Department of Physics, University of Ottawa, Ottawa, ON, K1N 6N5, Canada*

Jacob J. Krich

*Department of Physics, University of Ottawa, Ottawa, ON, K1N 6N5, Canada and  
School of Electrical Engineering and Computer Science,  
University of Ottawa, Ottawa, ON, K1N 6N5, Canada*

Nonlinear optical spectroscopies are powerful tools for probing quantum dynamics in molecular and nanoscale systems. While intuition about ultrafast spectroscopies is often built by considering infinitely short duration — impulsive — optical pulses, actual experiments have finite-duration pulses, which can be important for interpreting and predicting experimental results. We present a new freely available open source method for spectroscopic modeling, called Ultrafast Ultrafast (UF<sup>2</sup>) Spectroscopy, which enables computationally efficient and convenient prediction of nonlinear spectra, including treatment of arbitrary finite duration pulse shapes. We also present a Runge-Kutta Euler (RKE) direct propagation method, which is more efficient for systems with Hilbert space dimension greater than 100. These methods efficiently treat open systems with Markovian baths. For non-Markovian systems, the degrees of freedom corresponding to memory effects can be brought into the system, where they are treated nonperturbatively. UF<sup>2</sup> requires diagonalization of a system Liouvillian. While conventional wisdom dictates that such diagonalizations are too costly, we demonstrate that for important and frequently studied small systems, UF<sup>2</sup> can be over 500 times faster than the more standard RKE method. UF<sup>2</sup> and RKE are part of a larger open source Ultrafast Software Suite, which includes tools for automatic generation and calculation of Feynman diagrams.

## I. INTRODUCTION

Nonlinear optical spectroscopies (NLOS) are widely used tools for probing the excited state dynamics of a wide range of systems [1, 2]. The signals that can be measured using NLOS contain a wealth of information, but correctly interpreting that information generally requires making a model of the system and predicting the spectra that result. Such analysis can require repeated lengthy computations in order to fit multiple parameters to the collected data [3–6]. Fast methods for simulating spectra of model system enable better interpretation of experimental results.

NLOS are often calculated in the impulsive limit of infinitely short optical pulses. Recent work has shown that finite pulse effects can have dramatic effects on measured NLOS, and that fitting the data using intuition developed in the impulsive limit can lead to incorrect conclusions [7], adding to the existing body of work exploring the effects of finite pulse shapes [8–17]. The effects of Gaussian and exponential pulse shapes has been treated analytically for various types of NLOS, providing valuable insights into the effects of pulse shapes and durations [16, 17]. However, real experimental pulses are often not well represented by Gaussian or other analytical shapes. Ideally, modeling of NLOS should include actual experimental pulse shapes rather than approximate forms, and a number of numerical methods have this capability [8, 10, 18–22].

In Ref. [23] we introduced a novel fast algorithm based on Fourier convolution, called Ultrafast Ultrafast (UF<sup>2</sup>)

spectroscopy, capable of simulating any order NLOS using arbitrary pulse shapes. We compared it to our own implementation of a standard direct propagation method we called RKE (Runge-Kutta-Euler) and demonstrated that UF<sup>2</sup> shows a significant speed advantage over RKE for systems with a Hilbert space dimension smaller than 10<sup>4</sup>. However, that work is based upon wavefunctions and is only valid for closed systems. Condensed-phase systems in particular have essential dephasing and dissipation, making wavefunction methods of limited use in interpretation of experiments.

In this work we present the extension of both UF<sup>2</sup> and RKE to open quantum systems with Markovian baths. Degrees of freedom corresponding to memory in the bath can be included explicitly in the system Hamiltonian. We show that UF<sup>2</sup> is 500 times faster than RKE for small system sizes, and we believe this result is representative of the advantage that UF<sup>2</sup> provides over direct propagation methods. For open systems, UF<sup>2</sup> outperforms RKE until the system Hilbert space dimension  $N$  is approximately 100. Hereafter, the terms UF<sup>2</sup> and RKE refer to the new open extensions of the old algorithms of the same name, with the understanding that the closed system algorithms are now contained as special cases.

UF<sup>2</sup> works in the eigenbasis of the Liouvillian that propagates system density matrices and thus requires diagonalization of this Liouvillian. We show that, surprisingly, the cost of this diagonalization is negligible for the system sizes where UF<sup>2</sup> outperforms RKE, despite the Liouvillian having dimension  $N^2$ . Diagonalization yields fast, exact propagation of the unperturbed system and

allows the optical pulses to be included using the computational efficiency of the fast Fourier transform (FFT) and the convolution theorem.  $UF^2$  requires only that the pulse envelope be known at a discrete set of time points, and thus is able to study any pulse shape of interest, including experimentally measured pulse shapes. As few as 25 points are required with Gaussian pulses to obtain 1% convergence of spectra.

$UF^2$  and RKE are part of a software package we call the Ultrafast Spectroscopy Suite (UFSS), outlined in Fig. 1, which is designed to simplify the process of predicting spectra or fitting spectra to models. UFSS is designed in particular to facilitate inclusion of finite pulse effects with low computational cost. There are two distinct effects of finite pulses. First is the inclusion of additional Feynman diagrams that must be calculated when pulses overlap in time. UFSS includes an automated Feynman diagram generator (DG), described in Ref. 24, which automates the construction of these diagrams and determination of which ones give non-negligible contributions. Second is the calculation of the contribution from each diagram. Both  $UF^2$  and RKE take in diagrams and calculate their contributions including the effects of pulse shapes. UFSS also contains a Hamiltonian and Liouvillian generator (HLG), described in this manuscript, which parametrically constructs models for vibronic systems. Each of the packages in UFSS can be used independently. In this work we demonstrate how  $UF^2$  and RKE can be used separately, as well as with the HLG and DG. UFSS is free and open-source software written in Python, available for download from github.

In Sec. II we briefly review the formalism of NLOS calculated using time-dependent perturbation theory and then derive the  $UF^2$  and RKE algorithms. The computational complexity of these methods is shown in Appendix A. In Sec. III we describe the HLG and the systems it is built to describe. In Sec. IV we use the HLG to study and compare the computational cost of  $UF^2$  and RKE for a range of system sizes. In Sec. V we show the accuracy of  $UF^2$  by comparing to analytical expressions for the 2D photon echo signal of the optical Bloch equations perturbed by Gaussian pulses from Ref. 17. We demonstrate that  $UF^2$  converges to the analytical solution using just 25 evenly spaced points to represent the Gaussian pulse shape.

## II. ALGORITHM

We begin this section by outlining the standard results of time-dependent perturbation theory, and how it is applied to nonlinear optical spectroscopies [25], in order to introduce our notation and derive the formal operators that we use to describe signals. In Sec. IIA we build on this foundation to derive a novel open-systems algorithm called  $UF^2$  for calculating perturbative spectroscopies. In Sec. IIB we briefly present a direct propagation method called RKE that is included in UFSS, which is used as a

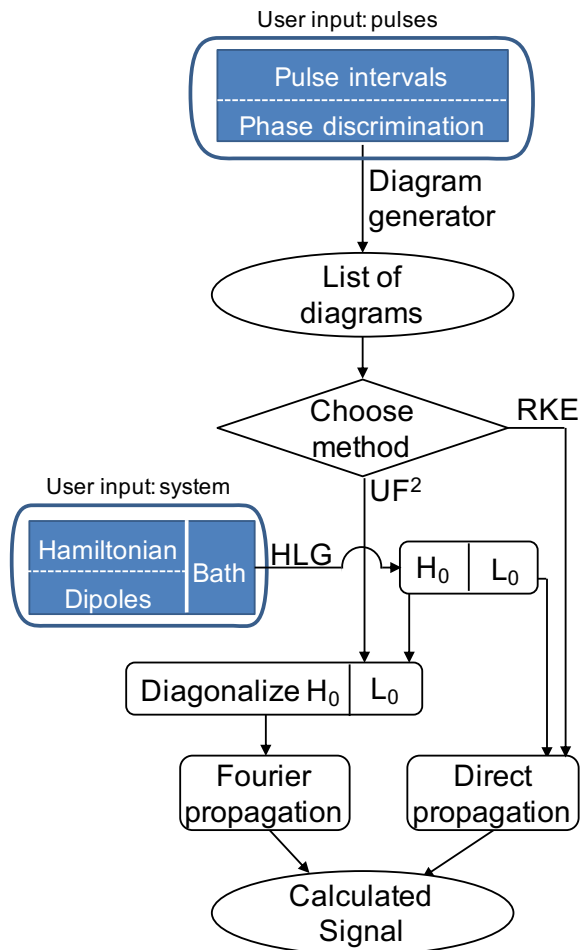


Figure 1. Logical flow of the UFSS package. Users input information about the experiment (pulse intervals and pulse-discrimination condition) and the system (states, optical dipoles, and system-bath interaction). UFSS consists of the diagram generator (DG), the Hamiltonian/Liouvillian generator (HLG), and two choices of propagators:  $UF^2$  and RKE. The DG produces a list of Feynman diagrams, as described in Ref. [24]. This list and the Hamiltonian or Liouvillian of the system are inputs to either  $UF^2$  or RKE, which calculate the contribution of each diagram to the resulting signal. The DG updates the list of diagrams as the pulse delay times change, so that  $UF^2$  and RKE only calculate causal diagrams for each set of pulse delays.

benchmark for timing comparisons with  $UF^2$ .

We begin with a Hamiltonian of the form

$$H = H_0(t) + H'(t), \quad (1)$$

where the light-matter interaction with a classical field  $\mathbf{E}(t)$  is treated perturbatively in the electric-dipole approximation as

$$H'(t) = -\boldsymbol{\mu} \cdot \mathbf{E}(t), \quad (2)$$

where  $\boldsymbol{\mu}$  is the electric dipole operator. Cartesian vectors are indicated in bold. We include a time-independent

system-bath interaction in the equations of motion for the system density matrix  $\rho$ , so

$$\frac{d\rho}{dt}(t) = -\frac{i}{\hbar}[H(t), \rho(t)] + D\rho(t), \quad (3)$$

where  $D$  is a superoperator that describes dephasing and dissipation. The UF<sup>2</sup> algorithm can be applied with any time-independent operator  $D$ . Separating the perturbation  $H'(t)$  yields two superoperators,  $\mathcal{L}_0$  and  $\mathcal{L}'(t)$ , which are defined as

$$\frac{d\rho}{dt}(t) = \underbrace{\frac{-i}{\hbar}([H_0, \rho(t)] + i\hbar D\rho(t))}_{\mathcal{L}_0|\rho(t)\rangle} + \underbrace{\frac{-i}{\hbar}[H'(t), \rho(t)]}_{\mathcal{L}'(t)|\rho(t)\rangle}. \quad (4)$$

$\rho$  can be considered as an operator in the Hilbert space of the material system  $\mathbb{H}$  and as a vector in the Liouville space  $\mathbb{L}$ , which is the vector space of linear operators on  $\mathbb{H}$ . We denote vectors in  $\mathbb{L}$  by  $|\cdot\rangle\rangle$ . For linear operators  $A$  and  $B$  acting on  $\mathbb{H}$ , we write the operator  $A \otimes B^T$  in  $\mathbb{L}$  such that  $A \otimes B^T|\rho\rangle\rangle$  is equivalent to  $A\rho B$ .<sup>1</sup> Using this transformation, we rewrite Eq. 4 as

$$\frac{d|\rho(t)\rangle\rangle}{dt} = \mathcal{L}_0|\rho(t)\rangle\rangle + \mathcal{L}'(t)|\rho(t)\rangle\rangle, \quad (5)$$

where, in terms of operators on  $\mathbb{H}$ ,

$$\mathcal{L}_0(t) = -\frac{i}{\hbar}H_0(t) \otimes \mathbb{I} + \frac{i}{\hbar}\mathbb{I} \otimes H_0^T(t) + i\hbar D(t) \quad (6)$$

and

$$\mathcal{L}'(t) = -\frac{i}{\hbar}\boldsymbol{\mu}^K \cdot \mathbf{E}(t) + \frac{i}{\hbar}\boldsymbol{\mu}^B \cdot \mathbf{E}(t), \quad (7)$$

with

$$\boldsymbol{\mu}^K = \boldsymbol{\mu} \otimes \mathbb{I} \quad \text{and} \quad \boldsymbol{\mu}^B = \mathbb{I} \otimes \boldsymbol{\mu}^T.$$

In a closed system,  $D = 0$ , and this formulation becomes equivalent to the closed case, which can be expressed with wavefunctions rather than density matrices [23].

We describe the electric field as a sum over  $L$  pulses, where each pulse is denoted by a lowercase letter starting from  $a$ . A typical  $3^{rd}$ -order signal is produced by up to 4 pulses. We write the electric field as

$$\mathbf{E}(t) = \sum_{j=a,b,\dots,L} \mathbf{e}_j \varepsilon_j(t) + \mathbf{e}_j^* \varepsilon_j^*(t) \quad (8)$$

<sup>1</sup> Note that the Liouville space is also a Hilbert space, with an inner product  $(v_1, v_2)$ , which can be expressed in terms of the inner product on  $\mathbb{H}$ . If  $|v_1\rangle\rangle = |a\rangle\langle b|$  and  $|v_2\rangle\rangle = |c\rangle\langle d|$ , then the inner product of  $v_1$  and  $v_2$  is  $\text{Tr}[v_1^\dagger v_2] = \langle d|b\rangle\langle a|c\rangle$ , where the trace is taken with respect to a Hilbert-space basis. All other cases following by linearity.

where  $\mathbf{e}_j$  is the possibly complex polarization vector, and the amplitude  $\varepsilon_j$  of each pulse is defined with envelope  $A_j$ , central frequency  $\omega_j$ , wavevector  $\mathbf{k}_j$ , and phase  $\phi_j$  as

$$\varepsilon_j(t) = A_j(t - t_j)e^{-i(\omega_j(t-t_j) - \mathbf{k}_j \cdot \mathbf{r} - \phi_j)},$$

where  $t_j$  is the arrival time of pulse  $j$ . We make the physical assumption that each pulse is localized in time so  $\varepsilon_j(t)$  is nonzero only for  $t \in [t_{j,\min}, t_{j,\max}]$ . For the purposes of UFSS,  $A_j(t)$  does not need to be a closed-form expression; it only needs to be known on a regularly spaced time grid in  $[t_{j,\min}, t_{j,\max}]$ . We define the Fourier transform of the pulse as

$$\tilde{\varepsilon}_i(\omega) = \int_{-\infty}^{\infty} \varepsilon_i(t)e^{i\omega t} dt.$$

The light-matter interaction, Eq. 7, is a sum over the rotating ( $\varepsilon_i$ ) and counter-rotating ( $\varepsilon_i^*$ ) terms. We express these terms individually as

$$\mathcal{L}'_{Kj^{(*)}}(t) = \frac{i}{\hbar}\boldsymbol{\mu}^K \cdot \mathbf{e}_j^{(*)}\varepsilon_j^{(*)}(t) \quad (9)$$

$$\mathcal{L}'_{Bj^{(*)}}(t) = -\frac{i}{\hbar}\boldsymbol{\mu}^B \cdot \mathbf{e}_j^{(*)}\varepsilon_j^{(*)}(t) \quad (10)$$

so that

$$\mathcal{L}'(t) = \sum_{i=a,b,\dots} \mathcal{L}'_{Ki}(t) + \mathcal{L}'_{Ki^*}(t) + \mathcal{L}'_{Bi}(t) + \mathcal{L}'_{Bi^*}(t). \quad (11)$$

In the rotating wave approximation (RWA), the rotating terms,  $\mathcal{L}'_{Ki}$  and  $\mathcal{L}'_{Bi}$ , excite the ket-side and de-excite the bra-side of the density matrix, respectively. The counter-rotating terms,  $\mathcal{L}'_{Ki^*}$  and  $\mathcal{L}'_{Bi^*}$ , excite the bra-side and de-excite the ket side, respectively [22, 25].

We treat the effect of  $\mathcal{L}'(t)$  using standard time-dependent perturbation theory and assume that at time  $t_0$  the system is in a stationary state of  $\mathcal{L}_0$ , which is  $|\rho^{(0)}\rangle\rangle$ . Equation 5 is easily integrated in the absence of perturbation to give the time-evolution due to  $\mathcal{L}_0$ ,

$$\mathcal{T}_0(t) = \exp[\mathcal{L}_0 t]. \quad (12)$$

The perturbation  $\mathcal{L}'(t)$  is zero before  $t_0$  and produces a time-dependent density matrix  $|\rho(t)\rangle\rangle$ , which is expanded perturbatively as

$$|\rho(t)\rangle\rangle = |\rho^{(0)}\rangle\rangle + |\rho^{(1)}(t)\rangle\rangle + |\rho^{(2)}\rangle\rangle + \dots \quad (13)$$

where the  $n^{\text{th}}$  term can be expressed as [25]

$$|\rho^{(n)}(t)\rangle\rangle = \mathcal{T}_0(t) \int_0^\infty dt' \mathcal{T}_0^{-1}(t-t') \mathcal{L}'(t-t') |\rho^{(n-1)}(t-t')\rangle\rangle.$$

Using the decomposition of  $\mathcal{L}'(t)$  in Eq. 11, we write  $|\rho^{(n+1)}(t)\rangle\rangle$  as a sum over four types of terms

$$|\rho^{(n+1)}(t)\rangle\rangle = \sum_j (K_j + K_{j^*} + B_j + B_{j^*}) |\rho^{(n)}(t)\rangle\rangle,$$

where all four terms are compactly defined as

$$O_{j^{(*)}} = \eta_O \frac{i}{\hbar} \mathcal{T}(t) \int_0^\infty dt' \mathcal{T}^{-1}(t-t') \left( \boldsymbol{\mu}^O \cdot \mathbf{e}_j^{(*)} \varepsilon_j^{(*)}(t-t') \right), \quad (14)$$

with  $O = K, B$ ,  $\eta_K = 1$  and  $\eta_B = -1$ , and the asterisk denotes the counter-rotating term.

From  $\rho^{(n)}(t)$ , perturbative signals can be determined. The full perturbative density matrix is given by

$$|\rho^{(n)}(t)\rangle\rangle = \left[ \sum_j (K_j + K_{j^*} + B_j + B_{j^*}) \right]^n |\rho^{(0)}\rangle\rangle, \quad (15)$$

which gives  $(4L)^n$  different terms, each of which is represented as a double-sided Feynman diagram. The number of diagrams that must be calculated can be dramatically reduced when considering the phase matching or phase cycling conditions in a particular spectrum, which are sensitive only to some of these contributions to  $\rho^{(n)}(t)$ . Further, many calculations are zero in the RWA. Time ordering also greatly reduces the number of required diagrams when the pulses do not overlap. There are well established methods to minimize the number of diagrams required to predict a spectrum, and Ref. [24] demonstrates how to automate that process.

Once the desired diagrams have been determined, the sum in Eq. 15 can be evaluated with only the relevant diagrams to produce the contributions to  $|\rho^{(n)}\rangle\rangle$  that produce the desired signal. For example, in the case of a phase-matching experiment with detector in the direction  $\mathbf{k}_d = \sum_j m_j \mathbf{k}_j$ , where  $m_j$  are integers, we call the portion of the density matrix that contributes to the signal  $\rho_{\mathbf{k}_d}^{(n)}$ . Then the signal  $S_{\mathbf{k}_d}^{(n)}$  is calculated using

$$\begin{aligned} \mathbf{P}_{\mathbf{k}_d}^{(n)}(t) &= \langle \boldsymbol{\mu} \rho_{\mathbf{k}_d}^{(n)}(t) \rangle \\ \tilde{\mathbf{P}}_{\mathbf{k}_d}^{(n)}(\omega) &= \int_{-\infty}^{\infty} dt e^{i\omega t} \mathbf{P}_{\mathbf{k}_d}^{(n)}(t) \\ S_{\mathbf{k}_d}^{(n)}(\omega) &= \text{Im} \left[ \tilde{\varepsilon}_d^*(\omega) \mathbf{e}_d \cdot \tilde{\mathbf{P}}_{\mathbf{k}_d}^{(n)}(\omega) \right] \end{aligned} \quad (16)$$

where  $\mathbf{P}_{\mathbf{k}_d}^{(n)}$  is the  $n^{\text{th}}$ -order polarization contributing to the desired signal and the final pulse, with electric field  $\mathbf{E}_d$ , is the local oscillator used to detect the radiated field. Figure 2 shows the diagrams contributing to the calculation of the rephasing two-dimensional photon echo (2DPE) signal when none of the pulses overlap.

The UF<sup>2</sup> and RKE methods each implement an operation of  $O_{j^{(*)}}$  on a density matrix. When they are given a diagram to evaluate, they compute the required successive  $O_{j^{(*)}}$  operations, for example  $B_c K_b B_{a^*} |\rho^{(0)}\rangle\rangle$ , which is the second diagram in Fig. 2.

### A. Novel open systems algorithm: UF<sup>2</sup>

We now describe the open systems algorithm we call UF<sup>2</sup> for the operators  $\{O_{j^{(*)}}\}$ , which is an extension of

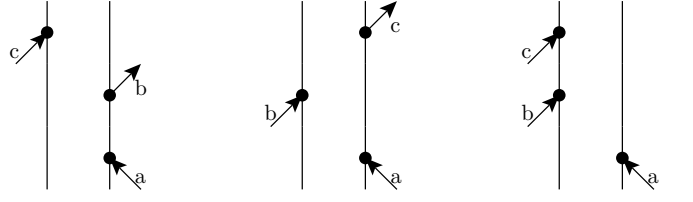


Figure 2. Time-ordered Feynman diagrams that contribute to the rephasing 2DPE, measured in the  $\mathbf{k}_d = -\mathbf{k}_a + \mathbf{k}_b + \mathbf{k}_c$  direction. Up to 13 other diagrams contribute to the signal when one or more of the pulses overlap [24].

the closed systems algorithm of the same name presented in Ref. 23. UF<sup>2</sup> requires that  $\mathcal{L}_0$  be time-independent and therefore that the bath be Markovian. All degrees of freedom corresponding to non-Markovian effects must be brought into the system, where they are treated non-perturbatively. With modest computational resource, we can include several explicit vibrational modes in the system, effectively giving highly accurate non-Markovian effects to a system that is formally treated as having a Markovian bath.

We diagonalize  $\mathcal{L}_0$  by finding the right and left eigenvectors. The right eigenvectors  $|\alpha\rangle\rangle$  form a basis and have eigenvalues  $z_\alpha$ , as

$$\mathcal{L}_0 |\alpha\rangle\rangle = z_\alpha |\alpha\rangle\rangle.$$

The left eigenvectors are defined using overbars as

$$\langle\langle \bar{\alpha} | \mathcal{L}_0 = \langle\langle \bar{\alpha} | z_\alpha.$$

Since  $\mathcal{L}_0$  need not be Hermitian,  $|\alpha\rangle\rangle^\dagger \neq \langle\langle \bar{\alpha} |$ . We normalize the left and right eigenvectors to satisfy

$$\langle\langle \bar{\alpha} | \beta \rangle\rangle = \delta_{\alpha\beta}. \quad (17)$$

In the absence of  $\mathcal{L}'(t)$ , Eq. 12 gives  $|\rho(t)\rangle\rangle = \mathcal{T}_0(t) |\rho(0)\rangle\rangle$ .  $\mathcal{T}_0$  is diagonal in the basis  $\{|\alpha\rangle\rangle\}$ , so we have

$$|\rho(t)\rangle\rangle = \sum_{\alpha} e^{z_\alpha t} c_\alpha |\alpha\rangle\rangle, \quad (18)$$

where  $N$  is the dimension of  $\mathbb{H}$ , which we take to be finite. If the physical system has an infinite dimensional  $\mathbb{H}$ , as in the case of a harmonic oscillator, we truncate  $\mathbb{H}$  to dimension  $N$ , and therefore truncate  $\mathcal{L}_0$  to dimension  $N^2$ .

The electric dipole operator acting from the left,  $\boldsymbol{\mu}^K$ , and from the right,  $\boldsymbol{\mu}^B$ , must be known in the eigenbasis of  $\mathcal{L}_0$ , where we define matrix elements

$$\begin{aligned} \boldsymbol{\mu}_{\alpha\beta}^K &= \langle\langle \bar{\alpha} | \boldsymbol{\mu}^K | \beta \rangle\rangle. \\ \boldsymbol{\mu}_{\alpha\beta}^B &= \langle\langle \bar{\alpha} | \boldsymbol{\mu}^B | \beta \rangle\rangle. \end{aligned}$$

The derivation of UF<sup>2</sup> for open systems is formally similar to that for closed systems in Ref. 23, with replacements of  $U$  by  $\mathcal{T}$ , the wavefunction  $|\psi\rangle$  by the density

vector  $|\rho\rangle\rangle$ , and the dipole operator  $\boldsymbol{\mu}$  by  $\boldsymbol{\mu}^K$  and  $\boldsymbol{\mu}^B$ . Because the action of the dipole operator on the ket and bra must be considered separately, the operator  $K_{j^{(*)}}$  is joined in the open systems case by its counterpart  $B_{j^{(*)}}$ .

We represent  $|\rho^{(n)}(t)\rangle\rangle$  with coefficients  $c_\alpha^{(n)}(t)$  that contain only the time dependence induced by the perturbation, while keeping the evolution due to  $\mathcal{L}_0$  separate

as

$$|\rho^{(n)}(t)\rangle\rangle = \sum_{\alpha} e^{z_{\alpha}t} c_{\alpha}^{(n)}(t) |\alpha\rangle\rangle.$$

With this notation, Eq. 14 gives

$$\begin{aligned} O_{j^{(*)}} |\rho^{(n)}(t)\rangle\rangle &= \eta_O \frac{i}{\hbar} \mathcal{T}_0(t) \int_0^{\infty} dt' \mathcal{T}_0^{-1}(t-t') \sum_{\beta} |\beta\rangle\rangle \langle\langle \bar{\beta} | \left( \boldsymbol{\mu}^O \cdot \mathbf{e}_j^{(*)} \varepsilon_j^{(*)}(t-t') \right) \sum_{\alpha} e^{z_{\alpha}(t-t')} c_{\alpha}^{(n)}(t-t') |\alpha\rangle\rangle \\ &= \eta_O \frac{i}{\hbar} \sum_{\beta} e^{z_{\beta}t} |\beta\rangle\rangle \int_{-\infty}^{\infty} dt' \theta(t') \underbrace{e^{-z_{\beta}(t-t')} \sum_{\alpha} \left( \boldsymbol{\mu}_{\beta\alpha}^O \cdot \mathbf{e}_j^{(*)} \varepsilon_j^{(*)}(t-t') \right) e^{z_{\alpha}(t-t')} c_{\alpha}^{(n)}(t-t')}_{y_{\beta}(t-t')}. \end{aligned} \quad (19)$$

The integral in Eq. 19 is a convolution, and we express it in the compact form

$$O_{j^{(*)}} |\rho^{(n)}(t)\rangle\rangle = \eta_O \frac{i}{\hbar} \sum_{\beta} e^{z_{\beta}t} |\beta\rangle\rangle [\theta * y_{\beta}](t), \quad (20)$$

where

$$[x * y](t) = \int_{-\infty}^{\infty} dt' x(t') y(t-t').$$

Assuming that  $\varepsilon_j(t)$  is zero outside the interval  $[t_{j,\min}, t_{j,\max}]$ ,

$$[\theta * y_{\beta}](t) = \begin{cases} 0 & t < t_{j,\min} \\ r_{\beta}(t) & t_{j,\min} < t < t_{j,\max} \\ C_{\beta} & t > t_{j,\max} \end{cases}.$$

for constant  $C_{\beta}$ . Therefore, we need only calculate this convolution for  $t_{j,\min} < t < t_{j,\max}$ .

Physically, we only need to solve for the time dependence due to the interaction with the pulse while the pulse is nonzero. The rest of the time dependence is contained in  $\mathcal{L}_0$  and is therefore known exactly. This realization drastically reduces the computational cost of UF<sup>2</sup> compared to techniques that must use time stepping for both the system dynamics and the perturbation.

We evaluate the convolution  $[\theta * y_{\beta}](t)$  numerically to solve for the function  $r_{\beta}(t)$  using the FFT and the convolution theorem. Each electric field envelope  $A_j(t-t_j)$  is represented using  $M_j$  equally spaced time points, where  $M_j = (t_{j,\max} - t_{j,\min})/dt_j$  and  $dt_j$  is the spacing between points. Before convolving  $y_{\beta}$  is zero-padded up to  $2M_j - 1$  points, and after the convolution is performed we retrieve only the  $M_j$  points corresponding to a linear convolution. Appendix A 1 describes the computational cost of UF<sup>2</sup> and shows how it scales with  $N$  and  $M$ .

## B. RKE

The RKE method is an alternative algorithm for evaluating the operators  $\{O_{j^{(*)}}\}$  and is also included in UFSS. It was introduced in Ref. 23 for closed systems. RKE uses the Runge-Kutta 45 (RK45) adaptive time step algorithm to propagate the evolution due to  $\mathcal{L}_0$  and a fixed-step Euler method to include the perturbation  $\mathcal{L}'(t)$ . It is a direct propagation method, meaning that it propagates  $|\rho\rangle\rangle$  forward one step at a time using the differential form of the equations of motion, Eq. 5. RKE is a simple example of a direct-propagation method, and we intend it to be representative of the computational scaling differences between UF<sup>2</sup> and direct-propagation methods; more efficient and higher-order methods than RKE are possible [2, 18, 21, 26–30].

In the absence of pulses, the RK45 method advances the density matrix  $|\rho\rangle\rangle$  forward in time according to

$$|\dot{\rho}\rangle\rangle = \mathcal{L}_0 |\rho\rangle\rangle \quad (21)$$

where we represent the time evolution due to  $\mathcal{L}_0$  as an  $N^2 \times N^2$  matrix acting on  $\mathbb{L}$ , rather than using  $N \times N$  operators on  $\mathbb{H}$  as in Eq. 3. We represent a step using the RK45 algorithm alone as  $|\rho(t_i + dt)\rangle\rangle = \mathcal{T}_0(dt) |\rho(t_i)\rangle\rangle$ .

Starting from  $|\rho^{(0)}\rangle\rangle$ , RKE evaluates diagrams by successive  $O_{j^{(*)}}$  operations. RKE calculates  $|\rho_{\beta}\rangle\rangle \equiv O_{j^{(*)}} |\rho_{\alpha}\rangle\rangle$  for some state  $|\rho_{\alpha}\rangle\rangle$  as

$$\begin{aligned} |\rho_{\beta}(t_{j,\min} + mdt_E)\rangle\rangle &= \mathcal{T}_0(dt_E) |\rho_{\beta}(t_{j,\min} + (m-1)dt_E)\rangle\rangle \\ &+ \mathcal{L}'_{O_{j^{(*)}}}(t_{j,\min} + mdt_E) |\rho_{\alpha}(t_{j,\min} + mdt_E)\rangle\rangle, \end{aligned} \quad (22)$$

where we propagate using fixed step size  $dt_E$  from  $t_{j,\min}$  to  $t_{j,\max}$ . This method accumulates error proportional to  $dt_E$ . It is possible to construct analogous methods that accumulate error proportional to  $dt_E^2$  [21]. Defining  $M_E = (t_{j,\max} - t_{j,\min})/dt$ ,  $m$  runs from 0 to  $M_E$ . Once

we obtain  $|\rho_\beta(t_{j,\max})\rangle\rangle$ , the remainder of the time evolution for  $t > t_{j,\max}$  is obtained using the standard RK45 method alone, with a variable time step.

### III. HAMILTONIAN/LIOUVILLIAN GENERATOR

Here we outline the Hamiltonian and Liouvillian generator (HLG) included as part of UFSS. Note that both UF<sup>2</sup> and RKE are compatible with any time-independent Hamiltonian or Liouvillian that can be expressed as a finite matrix. One need not use the HLG in order to take advantage of the other modules in UFSS.

HLG is a vibronic model generator, designed to create a Hamiltonian for a network of  $s$  two-level systems (2LS) coupled linearly to  $k$  harmonic vibrational modes. The HLG constructs a Liouvillian by including coupling of each degree of freedom to a Markovian bath using the Lindblad formalism. Models of this type have been used to describe many systems including conical intersections in pyrazine and energy transfer in photosynthetic complexes [31–34].

#### A. Hamiltonian Structure

We begin with an electronic system described by  $s$  2LS,

$$H_e = E_0 + \sum_{i=1}^s E_i a_i^\dagger a_i + \sum_{i \neq j} J_{ij} a_i^\dagger a_j,$$

where  $a_i$  is the annihilation operator for the excited state in the  $i^{\text{th}}$  2LS,  $E_i$  is the site energy,  $E_0$  is the ground state energy, and  $J_{ij}$  is a Hermitian matrix of electronic couplings. The system includes  $k$  explicit harmonic vibrational modes of frequency  $\omega_\alpha$ , generalized momentum  $p_\alpha$  and coordinate  $q_\alpha$  with Hamiltonian

$$H_{ph} = \frac{1}{2} \left( \sum_{\alpha=1}^k p_\alpha^2 + \omega_\alpha^2 q_\alpha^2 \right).$$

We treat standard linear coupling of these modes to the electronic system as

$$H_{e-ph} = \sum_{\alpha=1}^k \sum_{i=1}^s \omega_\alpha^2 d_{\alpha,i} q_\alpha a_i^\dagger a_i,$$

where  $d_{\alpha,i}$  indicates the coupling of each vibrational mode to each 2LS. It is related to the Huang-Rhys factor by

$$S_{\alpha,i} = \frac{1}{2} \omega_\alpha^2 d_{\alpha,i}^2.$$

The total system Hamiltonian is

$$H_0 = H_e + H_{ph} + H_{e-ph}. \quad (23)$$

If we work in the number basis of the vibrational modes, using the ladder operators  $b_\alpha$ , with  $q_\alpha = \frac{1}{\sqrt{2}}(b_\alpha + b_\alpha^\dagger)$ ,  $p_\alpha = \frac{i}{\sqrt{2}}(b_\alpha - b_\alpha^\dagger)$ , then  $H_0$  is highly sparse.  $H_{e-ph}$  has  $2k + 1$  entries per row.  $H_{ph}$  is formally infinite in size, so we truncate  $H_0$  to size  $N$  by fixing the total vibrational occupation number. Note that Eq. 23 is block diagonal with  $s + 1$  blocks. Each of these blocks is an optically separated manifold, and we index manifolds using  $X$  and  $Y$ , where  $X, Y$  can refer to the ground-state manifold (GSM), the singly excited manifold (SEM), the doubly excited manifold (DEM), and so on. Each block has a size  $N_X$ , and  $N = N_{GSM} + N_{SEM} + N_{DEM} + \dots$ . The block diagonal form of  $H_0$  is not required by UF<sup>2</sup>, but it allows useful simplifications in certain cases, which are discussed briefly at the end of this section and in Appendix A.

#### B. Liouvillian Structure

Using the Hamiltonian from Eq. 23, we construct the unitary part of the Liouvillian,  $\mathcal{L}_U = \mathcal{L}_0 - i\hbar D$ , where  $\mathcal{L}_0$  is defined in Eq. 6. We include coupling of a Markovian bath to all degrees of freedom of  $H_0$  using the Lindblad formalism [35]. If  $O$  is an operator on  $\mathbb{H}$ , then we use the superoperator

$$L[O]\rho = O\rho O^\dagger - \frac{1}{2} (O^\dagger O\rho + \rho O^\dagger O).$$

We consider dissipation in vibrational modes and both inter- and intra-manifold dephasing and relaxation of the electronic modes.

For vibrational mode  $\alpha$ , we describe coupling to the rest of the bath with the dissipation operator

$$D_v = \sum_{\alpha} \gamma_{v,\alpha} (N_{\text{th}} L[b_\alpha^\dagger] + (N_{\text{th}} + 1) L[b_\alpha]), \quad (24)$$

where  $\gamma_{v,\alpha}$  is the thermalization rate of the  $\alpha^{\text{th}}$  mode and  $N_{\text{th}} = \langle b_\alpha^\dagger b_\alpha \rangle = 1/(\exp(\beta\hbar\omega_\alpha) - 1)$  is the average number of excitations at equilibrium of a mode with energy  $\hbar\omega_\alpha$  coupled to a Markovian bath of temperature  $T$ , with  $\beta = 1/k_B T$ , with  $k_B$  the Boltzmann constant [35].

We describe inter-manifold electronic relaxation and the complementary incoherent thermal excitation processes with

$$D_{r1} = \sum_{i=1}^s \gamma_{r1,i} (C_{gi} L[a_i] + C_{ig} L[a_i^\dagger]),$$

where  $C_{ij} = \frac{e^{-\beta E_i}}{e^{-\beta E_i} + e^{-\beta E_j}}$ . Intra-manifold relaxation processes are described by

$$D_{r2} = \sum_{i \neq j} \gamma_{r2,ij} C_{ij} L[a_i^\dagger a_j].$$

Since  $C_{ij}/C_{ji} = e^{-\beta(E_i - E_j)}$ , we obtain a thermal distribution of eigenstates as  $t \rightarrow \infty$  if  $J_{ij} = 0$  and  $d_{i,\alpha} = 0$ .

Relaxation processes necessarily give rise to dephasing. We include additional intra-manifold dephasing using

$$D_{d2} = \sum_{i \neq j} \gamma_{d2,ij} L \left[ a_i^\dagger a_i - a_j^\dagger a_j \right].$$

All of the above processes also give rise to inter-manifold (optical) dephasing. We include additional, pure inter-manifold dephasing using

$$D_{d1} = \gamma_{d1} L \left[ \sum_{i=1}^s a_i^\dagger a_i \right]. \quad (25)$$

In the common case where  $\gamma_{d1}$  is larger than all the other bath coupling rates, the homogeneous linewidth(s) are dominated by the  $D_{d1}$  term. Putting all of these operators together we arrive at the total dissipation operator

$$D = D_{r1} + D_{r2} + D_{d1} + D_{d2} + D_\nu. \quad (26)$$

When working with optical spectroscopy,  $H_0$  is often block diagonal, and therefore the system is composed of distinct manifolds, as constructed in Sec. III A. In the case where we can also neglect inter-manifold relaxation processes ( $\gamma_{r1,i} = 0$ ), the total Liouvillian  $\mathcal{L}_0$  is also block diagonal. Under these assumptions  $\mathcal{L}_0$  can be arranged into blocks of size  $N_X^2 \times N_Y^2$ , allowing us to save both computational cost and memory, both for diagonalization (if applicable) as well as for use with UF<sup>2</sup> or RKE.

#### IV. COMPUTATIONAL ADVANTAGE

We compare the computational costs of the two UFSS propagation methods, UF<sup>2</sup> and RKE. We show that the convolution-based UF<sup>2</sup> can be up to 500 times faster than the direct-propagation RKE method for small systems, with the advantage persisting until  $N$  is approximately 100. In Appendix A 1, we derive the computational complexity of UF<sup>2</sup> and show that the cost of calculating the contribution from each diagram using UF<sup>2</sup> scales as  $N^4$  (see Eq. A3). In contrast, in Appendix A 2, we show that the cost of doing the same calculation using RKE scales as  $N^2$  (see Eq. A5). UF<sup>2</sup> has much more favorable prefactors, explaining its superior performance at smaller  $N$ . The derivation of the cost of RKE depends strongly on the sparse nature of vibronic systems when represented in the vibration occupation basis. For systems described by the HLG,  $H_0$  has approximately  $2k + 1$  nonzero entries per row,  $\mathcal{L}_U$  has  $2(2k + 1) - 1 = 4k + 1$  entries per row. The full  $\mathcal{L}_0 = \mathcal{L}_U + i\hbar D$  has slightly more entries. With dense  $\mathcal{L}_0$ , the cost of RKE scales as  $N^3$ . In such a case, the crossover would likely occur for larger  $N$  than reported here.

UF<sup>2</sup> also has the additional one-time cost of the diagonalization of  $\mathcal{L}_0$ , which scales as  $N^6$ . Despite being an expensive calculation, it does not necessarily contribute significantly to the total cost of calculating spectra, because it is reused for each set of pulse delays, pulse

shapes, pulse polarizations, etc. It need only be redone if the parameters of  $H_0$  or  $\mathcal{L}_0$  are changed. Consider a sample 2DPE signal  $S^{(3)}(\tau, T, \omega_t)$  with 100 coherence times  $\tau$  and 20 population times  $T$ , as well as a sample TA signal  $S^{(3)}(T, \omega_t)$  with 100 delay times. Since the 2DPE spectrum requires 3-16 diagrams evaluated with 2000 different pulse delays, the cost of the diagonalization is effectively amortized over  $> 6000$  calculations. The TA calculation requires 6-16 diagrams evaluated at only 100 delay times, so amortizes the diagonalization cost only over  $\approx 600$  calculations. The RKE method does not require diagonalization, so the system size at which it becomes cost effective to use the RKE method in principle depends on what type of spectrum is being considered. In fact, we find that the diagonalization time is insignificant until approximately the system size at which RKE starts to outperform UF<sup>2</sup> without consideration of diagonalization. Therefore and surprisingly we deem the cost of diagonalization to be relatively unimportant when choosing a propagation method.

The computational costs of predicting spectra depend not only upon the size but also the structure of the Liouvillian that describes the problem. To make concrete comparisons between UF<sup>2</sup> and RKE, we use a vibronic Hamiltonian  $H_0$  coupled to a Markovian bath, as outlined in Section III. Figure 3 shows the ratio of the computation time of RKE to the computation time of UF<sup>2</sup> for TA spectra with a variety of vibronic systems. We considered systems with the number of sites and number of vibrational modes equal ( $s = k$ ) and varying from 2 to 4. The energy scale of the problem is defined by the  $k$  identical vibrational frequencies  $\omega_\alpha = \omega_0$ . The site energies  $E_i$  varied from  $0 - 1.5\omega_0^{-1}$  (where the optical gap has been rotated away), and the coupling terms  $J_{ij}$  varied from  $0 - 0.5\omega_0^{-1}$ . We used the same value of  $d_{\alpha,i} = d\delta_{\alpha,i}$  for each  $\alpha, i$  pair, where  $\delta_{i,j}$  is the Kronecker delta, and chose five values of  $d$  from 0 to 0.2. Larger values of  $d$  require a larger truncation size  $N$  for the spectra to converge. We included a Markovian bath using  $\gamma_{r2,i} = 0.05\omega_0^{-1}$ ,  $\gamma_{\nu,\alpha} = 0.05\omega_0^{-1}$  and  $\gamma_{d1} = 0.2\omega_0^{-1}$  (with  $\gamma_{r1} = \gamma_{d2} = 0$ ). The optical pulses were modeled as Gaussians of standard deviation  $\sigma = \omega_0^{-1}$ , centered on the transition  $E_1 - E_0$ . All sites  $i$  were taken to have parallel, equal-magnitude dipole moments, and we took the Condon approximation.

We chose the number of vibrational states in the simulations to be sufficiently large by using UF<sup>2</sup> to generate a TA signal and seeking the truncation size  $N$  that converges the resulting spectra within 1% using an  $\ell_2$  norm over the full spectrum. We performed this convergence separately for each case of  $s, d$ . We used the same value of  $N$  for the RKE calculations. The optical field parameters ( $M$  and  $dt$  for UF<sup>2</sup> and  $M_E$  and  $dt_E$ ) were determined by testing on some of the smaller systems and were held constant for all  $s, d$ . Values of  $t$  were selected in order to resolve all optical oscillation frequencies in the RWA and to resolve the homogeneous linewidth, which is dominated by the term  $\gamma_{d1,i} = 0.2\omega_0$ . We took the inter-manifold

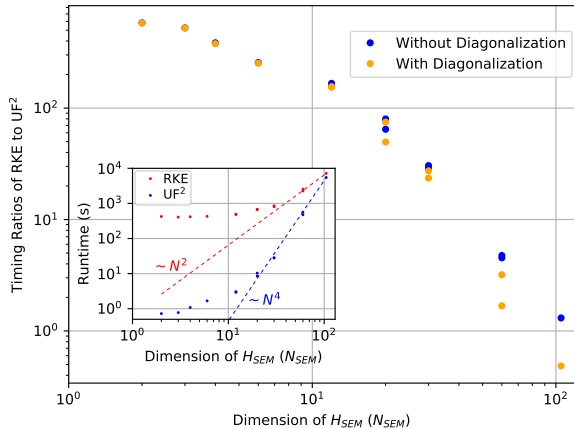


Figure 3. Timing ratios of RKE to  $UF^2$  methods for TA spectra with 100 time delays for a range of systems and parameters, described in the text.  $N_{SEM}$  is the dimension of the Hamiltonian describing the truncated singly excited manifold, large enough to converge the spectra. Blue points show the timing ratios for the evaluation of the spectra but not the diagonalization of  $\mathcal{L}_0$ . Orange points include the cost of the diagonalization, which is insignificant with small  $N_{SEM}$ . Near  $N_{SEM} = 100$ , the direct-propagation RKE method becomes more efficient than  $UF^2$ . Inset shows the time required to calculate the TA spectrum using RKE and  $UF^2$ , without the diagonalization cost included. The dashed lines show the slopes of the predicted asymptotic scaling of each algorithm. All calculations were performed on an Intel Xeon E5-2640 v4 CPU with a 2.40 GHz clock speed.

relaxation rate  $\gamma_{\tau 1} = 0$ , so that the optical manifolds are separable and  $\mathcal{L}_0$  is block diagonal.

Figure 3 demonstrates that for small  $N_{SEM}$ ,  $UF^2$  is about 500 times faster than RKE. The inset shows the actual runtimes for each value of  $N_{SEM}$ , not including the diagonalization cost for  $UF^2$ . The dashed lines in the inset show that as  $N_{SEM}$  increases, the expected asymptotic scalings derived in Appendix A are observed. The different asymptotic scalings lead to the crossover in runtimes that occurs around  $N_{SEM} = 100$ , corresponding to  $\mathcal{L}_0$  having blocks of dimension  $N_{SEM}^2 = 10^4$ . This crossover is consistent with our result with closed systems in Ref. 23, where the  $UF^2$  method was more efficient than RKE for  $N_{SEM}$  smaller than  $10^4 - 10^5$ . For small  $N_{SEM}$ , the cost of diagonalization is negligible, as shown by the blue and orange dots in Figure 3 all overlapping for  $N_{SEM} < 10$ . As  $N_{SEM}$  increases, the cost of diagonalization becomes apparent as the colors separate. With or without diagonalization, Fig. 3 shows that the crossover occurs with  $N_{SEM} \approx 100$ .

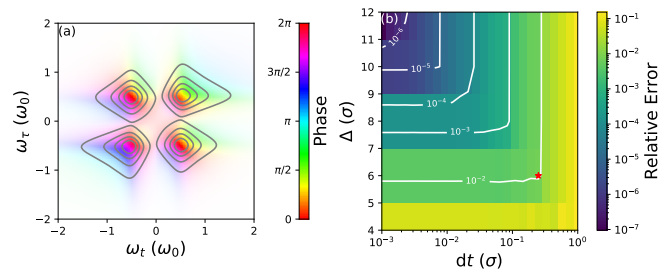


Figure 4. (a) Reproduction of Smallwood's Figure 3e) using their analytical forms. The color shows the phase of the complex signal  $P^{(3)}(\omega_\tau, T, \omega_t)$ , while the intensity of the color shows the magnitude of the signal. The numerical result using  $UF^2$  appears visually identical so is not shown. (b)  $\ell_2$  norm of the difference between the analytical solution shown in (a) and the result from  $UF^2$ , both sampled on a mesh of  $801 \times 801$   $\omega_t, \omega_\tau$  points, as a function of  $dt$  and the pulse duration  $\Delta$  used in the numerical convolutions of Eq. 20. We evaluate  $P^{(3)}(\tau, T, t)$  for  $t$  and  $\tau$  ranging from  $-100\sigma$  to  $100\sigma$  in steps of  $0.25\sigma$ . The red star in (b) indicates the smallest value of  $M = \Delta/dt + 1$  needed to reach 1% agreement with the analytical solution shown in (a), and corresponds to  $M = 25$  points. Note that for  $\Delta = 12\sigma$ , the figure shows that  $UF^2$  converges to the analytical signal as  $dt^2$ .

## V. COMPARISON OF $UF^2$ TO ANALYTIC RESULTS

We now demonstrate that the signals produced by  $UF^2$  reproduce an analytical solution for the rephasing 2D photon echo (2DPE) signal for the optical Bloch equations using Gaussian pulses [17]. The analytical solution provides a benchmark to show that  $UF^2$  calculates spectra with a high degree of accuracy.  $UF^2$  converges to within 1% of the analytical result using just  $M = 25$  points to discretize  $\varepsilon_j(t)$ . The model studied in Ref. 17 can be mapped to the Hamiltonian described by  $s = 2$  and  $k = 0$  from Sec. III, with the doubly excited state removed. In this model, the energy difference between the two excited states is  $\hbar\omega_0 = E_2 - E_1$ . All pulses are taken to have identical Gaussians envelopes

$$A(t) = \frac{1}{\sqrt{2\pi}\sigma} e^{-t^2/2\sigma^2},$$

where  $\sigma = \omega_0^{-1}$ . All pulses are centered on  $\omega_j = (E_2 + E_1)/(2\hbar)$ . In the RWA, we are free to set  $\omega_j = 0$  for all pulses, which we do. The model includes phenomenological population decay and dephasing rates of  $0.1\omega_0$  and  $0.2\omega_0$ , respectively. This bath coupling is similar to that outlined in Sec. IIIB, except that it does not conserve the total probability of the density matrix. Rather than using the HLG included in UFSS, for this comparison we separately created the model described in Ref. 17. The construction of  $\mathcal{L}_0$  and the evaluation of the resulting spectra is demonstrated in the jupyter notebook `Smallwood2017Comparison.ipynb`, available in the UFSS repository.

The 2DPE signal is the result of three pulses, which gives rise to an emitted field  $P(\tau, T, t)$ . UF<sup>2</sup> is designed to calculate  $P(\tau, T, t)$ , while the result from Ref. 17 is for the quantity

$$P(\omega_\tau, T, \omega_t) = \frac{1}{2\pi} \int_{-\infty}^{\infty} dt e^{i\omega_t t} \int_{-\infty}^{\infty} d\tau e^{-i\omega_\tau \tau} P(\tau, T, t).$$

To compare UF<sup>2</sup> to the analytical solutions, we calculate  $P(\tau, T, t)$  for a discrete set of  $\tau, T, t$ , and take a 2D discrete Fourier transform with respect to  $\tau$  and  $t$ . Since  $A(t)$  is symmetric, we evaluate  $A(t - t_j)$  on the interval  $t \in [t_{j,\min}, t_{j,\max}]$  with spacing  $dt$ , and choose  $t_{j,\max} - t_j = t_j - t_{j,\min}$ , where  $t_j$  is the arrival time of the  $j^{\text{th}}$  pulse. For symmetric pulses, UF<sup>2</sup> converges most rapidly when the value  $t - t_j = 0$  is included at the center of the discretization interval and the endpoints of the interval are also included. We define the duration of the pulse,  $\Delta_j \equiv t_{j,\max} - t_{j,\min}$  and the number of points  $M_j = \Delta_j/dt + 1$ . All the pulses are identical, and so we use  $M = M_j$ , and therefore  $\Delta = \Delta_j$  for each pulse.

Figure 4(a) shows the analytical result for  $P(\omega_\tau, 0, \omega_t)$ , which provides a benchmark for quantifying the convergence behavior of UF<sup>2</sup>. Fig. 4(b) shows the  $\ell_2$  norm of the difference between the analytical solution shown in (a) and the result from UF<sup>2</sup>. The white contours in Fig. 4(b) show that the errors due to  $\Delta$  and  $dt$  are nearly independent, since the contours are approximately composed of horizontal and vertical lines, leading to the appearance of terraces in the color plot. Inspection of the top of that plot show that UF<sup>2</sup> converges to the analytical signal as  $dt^2$ , when  $\Delta$  is sufficiently large that only the error from  $dt$  is significant. UF<sup>2</sup> reproduces the analytical result to within 1% by using  $\Delta = 6\sigma$  and  $dt = 0.25\sigma$ , corresponding to  $M = 25$ . The spectra attained using these parameters is not shown, as it is visually identical to Fig. 4(a). We conclude that UF<sup>2</sup> accurately predicts nonlinear optical spectra with small  $M$ .

## VI. CONCLUSION

We have presented three separate components of the Ultrafast Spectroscopy Suite (UFSS), which is a modular suite of tools designed for predicting nonlinear optical spectra. We have presented a novel algorithm called UF<sup>2</sup> that uses the convolution theorem to efficiently propagate the time evolution of eigenstates of the system Liouvillian. UF<sup>2</sup> is designed for evaluating the contributions to spectroscopic signals from the Feynman diagrams that organize perturbative calculations of nonlinear optical spectra. UF<sup>2</sup> is the open-systems extension of the closed-system algorithm of the same name presented in Ref. 23. We have also presented a direct propagation technique called RKE and a Hamiltonian/Liouvillian generator (HLG), which creates Hamiltonians and Liouvillians for vibronic systems coupled to a Markovian bath. Using the HLG, we have demonstrated that UF<sup>2</sup>

can be over 500 times faster than RKE for systems with small Hilbert space dimension  $N$ . For  $N \approx 100$ , RKE begins to outperform UF<sup>2</sup>. Both methods are available with UFSS and can be used where appropriate.

A fourth module of UFSS, called the diagram generator (DG), is presented in Ref. [24]. The DG automatically generates all of the necessary Feynman diagrams that are needed to calculate a spectroscopic signal given the phase-matching (or phase-cycling) condition, the pulse shapes and pulse arrival times. Taken all together, the UFSS allows fast and automated calculations of nonlinear optical spectra of any perturbative order, for arbitrary pulse shapes, since UF<sup>2</sup> and RKE can both automatically calculate spectra given a list of Feynman diagrams. If desired, a user of UFSS need not concern themselves with the details of the perturbative calculations carried out by UF<sup>2</sup> and RKE. They simply must input the phase-matching conditions and pulse shapes of interest.

Each module of UFSS presented here can also be used separately. UF<sup>2</sup> and RKE can calculate the signal due to only a single Feynman diagram, or only the time-ordered diagrams, as is done when comparing to the analytical results of Ref. 17. UF<sup>2</sup> and RKE are compatible with any Hamiltonian or Liouvillian that is time-independent and can be expressed as or well-approximated by a finite matrix. Thus users are free to input their own model systems, and we include helper functions for saving other Hamiltonians and Liouvillians into a format compatible with UF<sup>2</sup> and RKE.

UFSS is available under the MIT license at github. The repository includes jupyter notebooks that generate Figures 2 and 4 from this manuscript and scripts that generate Figure 3.

## ACKNOWLEDGMENTS

We acknowledge support from the Natural Sciences and Engineering Research Council of Canada (NSERC) and the Ontario Trillium Scholarship.

## Data Availability Statement

The data that support the findings of this study are available from the corresponding author upon reasonable request.

## Appendix A: Computational cost

Here we derive the asymptotic computational cost of both UF<sup>2</sup> and RKE. We derive the computational cost of calculating the signal  $S_d^{(n)}$  due to a single Feynman diagram for each algorithm, which we call  $C_{\text{UF}^2}(S_d^{(n)})$  and  $C_{\text{RKE}}(S_d^{(n)})$ . This cost is the cost of calling  $O_{j^{(*)}}$   $n$  times

to arrive at  $|\rho_d^{(n)}(t)\rangle\rangle$ , plus the additional cost of calculating the signal  $S_d^{(n)}$  from  $|\rho_d^{(n)}(t)\rangle\rangle$ , as in, for example, Eq. 16. If the RWA holds, and there are well-defined manifolds (ground-state, singly excited, doubly excited, etc.) such that only the optical perturbations couple between them on the timescales of interest, then the density matrix and Liouvillian can be broken into smaller pieces. We derive the cost of the general case where the manifolds are not separable and then extend the result to separable manifolds. We show that the cost of UF<sup>2</sup> is dominated by the cost of full matrix-vector multiplications, which must be used to apply the dipole operator to states in the eigenbasis of  $\mathcal{L}_0$ . RKE can use the vibrational number basis and thus keeps the dipole matrix sparse, but its time propagation is more expensive.

For an arbitrary  $n^{\text{th}}$ -order spectroscopy, both UF<sup>2</sup> and RKE must calculate the same number of diagrams. Since the total number of diagrams affects the total runtime of each algorithm and not the ratio of the runtimes, we consider the cost of only one diagram here.

### 1. UF<sup>2</sup>

For UF<sup>2</sup>, each call of the  $O_{j^{(*)}}$  operators is dominated by two operations: (1) multiplying the old state by the dipole operator to obtain  $y_\beta(t)$  (see Eq. 19), and (2) performing the convolution  $\theta(t) * y_\beta(t)$  using the FFT (see Eq. 20). The cost of both of these operations depends on the model system being studied. In the general case with inter-manifold relaxation processes, all density matrices are expressed as vectors of length  $N^2$ :

$$|\rho\rangle\rangle = \sum_{\alpha} c_{\alpha}(t) e^{z_{\alpha}t} |\alpha\rangle\rangle,$$

and all the operators on this space,  $\mathcal{L}_0$ ,  $\boldsymbol{\mu}^K \cdot \mathbf{e}_i$ ,  $\boldsymbol{\mu}^B \cdot \mathbf{e}_i$ , are  $N^2 \times N^2$  matrices. Given  $|\rho^{(n-1)}(t)\rangle\rangle$ , the first step in determining  $|\rho_d^{(n)}(t)\rangle\rangle = O_{j^{(*)}} |\rho^{(n-1)}(t)\rangle\rangle$  is to determine the coefficients  $y_\beta(t)$  at  $M$  time points, where  $M$  must be large enough to well-represent the pulse envelope shape  $A(t)$ , see Fig. 4. This cost is the cost of the matrix-vector multiplication  $\mu^O |\rho\rangle\rangle$  performed  $M$  times,

$$C(\mu^O |\rho(t)\rangle\rangle) = aN^4 M,$$

where  $a$  is the cost of multiplying two complex numbers. The next step, calculating the convolutions  $\theta(t) * y_\beta(t)$  using the FFT, is

$$C(\theta(t) * y_\beta(t)) = bM \log_2 M,$$

where  $b$  depends upon the implementation of the FFT.  $\beta$  indexes the  $N^2$  elements of the vector so the total cost of  $O_{j^{(*)}}$  is

$$C(O_{j^{(*)}}) = aN^4 M + bN^2 M \log_2 M. \quad (\text{A1})$$

Since we are most interested in the asymptotic scaling with  $N$ , we have

$$C(O_{j^{(*)}}) \sim N^4 M.$$

For an  $n^{\text{th}}$ -order spectroscopy, each Feynman diagram describes an  $n^{\text{th}}$ -order density matrix. Starting from the unperturbed density matrix  $|\rho^{(0)}\rangle\rangle$ , we require  $n$  calls to the  $O_{j^{(*)}}$  operator, and so the cost of obtaining  $|\rho_d^{(n)}(t)\rangle\rangle$  from  $|\rho^{(0)}\rangle\rangle$  is  $nC(O_{j^{(*)}})$ . This cost accrues for a single set of pulse delays. Since the calculations of  $|\rho^{(n-1)}(t)\rangle\rangle$  can be reused, the most expensive part of calculating a multidimensional spectrum is varying the last pulse delay. We discussed this scaling in Appendix A of Ref. 23, and the same arguments apply here.

In order to calculate the desired signal  $S_d$  from  $|\rho_d^{(n)}(t)\rangle\rangle$ , the density matrix must be evaluated at a single time point (in the case of integrated measurements, as in phase-cycling experiments) or at the  $M + m_t$  time points that determine  $P_d^{(n)}(t)$  (as in Eq. 16 for phase-matching experiments).  $M$  time points are needed to resolve the turn-on of the signal, governed by the pulse envelope shape  $A(t)$ , and  $m_t$  is determined by the optical dephasing rate(s) and the desired frequency resolution of the final signal. Since  $P_d^{(n)}(t) = \text{Tr}[\boldsymbol{\mu} \rho_d^{(n)}(t)]$ , taking the trace at  $M + m_t$  points has a cost of  $aN^4(M + m_t)$ , dominated again by the matrix-vector multiplication. For polarization-based signals,

$$C(P_d^{(n)}(t)) \sim \underbrace{N^4 M}_{C(O_{j^{(*)}})} + \underbrace{N^4(M + m_t)}_{C(\text{Tr}[\boldsymbol{\mu} \rho_f^{(n)}(t)])}. \quad (\text{A2})$$

The cost of taking the FFT of  $P_d^{(n)}(t)$  to obtain  $S_d^{(n)}(\omega)$  does not depend on  $N$  and is negligible. Thus

$$C_{\text{UF}^2}(S_d^{(n)}) \sim N^4(2M + m_t) \quad (\text{A3})$$

per set of pulse delay times. Calculating the polarization from  $|\rho_d^{(n)}(t)\rangle\rangle$  can be more expensive than constructing  $|\rho_d^{(n)}(t)\rangle\rangle$ . For phase-cycling cases, the cost is only  $\sim N^4 M$ .

In the case of separable manifolds, we note that the leading  $N^4$ -dependence in the cost comes from the matrix multiplications in  $C(\mu^O |\rho\rangle\rangle)$  and in  $C(P_d^{(n)}(t))$ . In the case of separable manifolds,  $\mathcal{L}_0$  is block diagonal, with blocks of shape  $N_X N_Y \times N_X N_Y$ , where  $X$  and  $Y$  are manifold indices as in Sec. III A. In this case  $|\rho\rangle\rangle$  exists either in a manifold,  $X$ , or in a coherence between two manifolds  $X, Y$ . We thus replace  $|\rho\rangle\rangle$  by  $|\rho_{XY}\rangle\rangle$ , where when  $X = Y$ , the density matrix is in a manifold. The dipole operators  $\boldsymbol{\mu}^K$  and  $\boldsymbol{\mu}^B$  connect  $|\rho_{XY}\rangle\rangle$  to  $|\rho_{X'Y'}\rangle\rangle$  and  $|\rho_{XY'}\rangle\rangle$ , respectively, and have shapes  $N_{X'} N_{Y'} \times N_X N_Y$ , where for  $\mu^K$ ,  $Y = Y'$ , and for  $\mu^B$ ,  $X = X'$ . Thus we can replace all occurrences of  $N^4$  with  $N_X N_Y N_{X'} N_{Y'}$ . Since  $X, X', Y, Y'$  are dummy indices,

and we have that either  $X = X'$  or  $Y = Y'$ , we simplify slightly to

$$C_{\text{UF}^2}(S_d^{(n)}) = aN_X^2 N_Y N_{Y'} (2M + m_t).$$

Note that for third-order spectroscopies, every diagram describes a density matrix  $\rho_f^{(3)}$  that ends in a coherence between either the GSM and the SEM, or the SEM and the DEM. As we discuss in Ref. 23, the most costly calculation for TA and 2DPE calculations is the excited-state absorption (ESA), due to the increased number of states in the excited manifolds of vibronic systems with  $s > 2$ . That diagram involves  $X = SEM, Y = DEM, Y' = SEM$ , so

$$C_{\text{UF}^2}(ESA) = N_{SEM}^3 N_{DEM} (2M + m_t), \quad (\text{A4})$$

which is why we plot runtimes and runtime ratios against  $N_{SEM}$ .

## 2. RKE

For RKE, each call to  $O_{j^{(*)}}$  (1) uses the Euler method to connect  $\rho^{(n-1)}$  to  $\rho^{(n)}$  via Eq. 22 while the pulse is non-zero, and (2) extends the density matrix beyond  $t_{j,\max}$  using the RK45 method to solve the ODE given by Eq. 21. RKE represents  $|\rho\rangle\rangle$  in the site and vibration-number basis, ie., the basis in which  $H_0$  is naturally defined. In this basis,  $H_0$  is sparse, and  $\mathcal{L}_0$  and  $\mu^O$  are also sparse. For the purposes of comparing to  $\text{UF}^2$ , we represent the time evolution due to  $\mathcal{L}_0$  as an  $N^2 \times N^2$  matrix, using Eq. 5 (with  $\mathcal{L}' = 0$ ) rather than using  $N \times N$  operators as in Eq. 3. Equation 5 involves the same or fewer operations. Equation 5 does require more memory to evaluate than Eq. 3, but we are not considering memory requirements here.

Given any state  $|\rho\rangle\rangle$ , the cost of the evolution according to Eq. 5 when  $\mathcal{L}'(t) = 0$  is the cost of multiplying the vector  $|\rho\rangle\rangle$  by the sparse matrix  $\mathcal{L}_0$ . Assuming that  $\mathcal{L}_0$  has  $r$  nonzero entries per row, the cost of each time step is  $C_{RK} = 6a(qr + 1)N^2 \approx 6\alpha qrN^2$ , where  $q$  is a factor representing sparse matrix overhead and the factor of 6

comes from the number of function evaluations required by the RK45 algorithm. Given a local tolerance  $\epsilon$ , the RK45 algorithm takes adaptive steps of size  $dt_{RK}$ . We approximate  $dt_{RK}$  as a constant and neglect the additional cost incurred when a step is rejected.

Given  $|\rho^{(n-1)}(t)\rangle\rangle$ , the cost of determining  $|\rho^{(n)}(t)\rangle\rangle$  from  $t_{j,\min}$  to  $t_{j,\max}$  is the cost of the two main ingredients: including the pulse via the operation  $\mu^O|\rho^{(n-1)}\rangle\rangle$ , which involves multiplying the vector  $|\rho^{(n-1)}\rangle\rangle$  by a sparse object  $\mu^O$  with a mean number of entries per row  $r_\mu$ , and a call to the RK45 algorithm with cost  $C_{RK}$ . We divide the interval  $[t_{j,\min}, t_{j,\max}]$  into  $M_E$  time points with equal spacing  $dt_E$ . Thus the cost of determining  $|\rho^{(n)}(t)\rangle\rangle$  from  $t_{j,\min}$  to  $t_{j,\max}$  is

$$C_{\text{pulse}} = \left( \underbrace{aqr_\mu N^2}_{C_\mu} + \underbrace{aq6rN^2}_{C_{RK}} \right) M_E,$$

where we have assumed that  $dt_E < dt_{RK}$ . In the Condon approximation,  $r_\mu$  is close to 1, while  $r$  is  $O(10)$ , so  $C_\mu < 10C_{RK}$  and we can neglect it.

From  $t_{j,\max}$  to some final time  $t_f$ , the RK45 algorithm advances the density matrix forward in time with cost  $C_{RK}M_{RK}$ , where  $M_{RK} = (t_f - t_{j,\max})/dt_{RK}$ .

$$C_{RKE}(O_{j^{(*)}}) = C_{\text{pulse}} + C_{RK}M_{RK}.$$

By comparison with Eq. A1, we see that density matrix propagation asymptotically benefits from the sparsity of  $\mathcal{L}_0$  and  $\mu^O$ , reducing the  $N^4$  scaling to  $N^2$ .

If manifolds are separable,  $|\rho_d^{(n)}(t)\rangle\rangle$  is of length  $N_X N_Y$ , so we can replace all occurrences of  $N^2$  with  $N_X N_Y$ , giving

$$C_{RKE}(S_d^{(n)}) \sim N_X N_Y (M_E + M_{RK}). \quad (\text{A5})$$

As mentioned in Appendix A1, the most costly calculation for TA and 2DPE calculations is the ESA, which involves  $X = SEM, Y = DEM$ , so

$$C_{RKE}(ESA) = N_{SEM} N_{DEM} (M_E + M_{RK}). \quad (\text{A6})$$

- 
- [1] D. Abramavicius, B. Palmieri, D. V. Voronine, F. Šanda, and S. Mukamel, *Chemical Reviews* **109**, 2350 (2009).
- [2] W. Domcke and G. Stock, "Theory of ultrafast nonadiabatic excited-state processes and their spectroscopic detection in real time," in *Advances in Chemical Physics* (John Wiley & Sons, Ltd, 2007) pp. 1–169.
- [3] M. Cho, H. M. Vaswani, T. Brixner, J. Stenger, and G. R. Fleming, *The Journal of Physical Chemistry B* **109**, 10542 (2005).
- [4] J. Adolphs, F. Müh, M. E.-A. Madjet, and T. Renger, *Photosynthesis Research* **95**, 197 (2007).
- [5] F. Müh, M. E.-A. Madjet, J. Adolphs, A. Abdurahman, B. Rabenstein, H. Ishikita, E.-W. Knapp, and T. Renger, *Proceedings of the National Academy of Sciences* **104**, 16862 (2007).
- [6] A. Perdomo-Ortiz, J. R. Widom, G. A. Lott, A. Aspuru-Guzik, and A. H. Marcus, *J. Phys. Chem. B* **116**, 10757 (2012).
- [7] D. Paleček, P. Edlund, E. Gustavsson, S. Westenhoff, and D. Zigmantas, *The Journal of Chemical Physics* **151**, 024201 (2019).
- [8] S. M. Gallagher Faeder and D. M. Jonas, *The Journal of Physical Chemistry A* **103**, 10489 (1999).
- [9] D. M. Jonas, *Annual Review of Physical Chemistry* **54**,

- 425 (2003).
- [10] N. Belabas and D. M. Jonas, *Opt. Lett.* **29**, 1811 (2004).
- [11] P. F. Tekavec, J. A. Myers, K. L. M. Lewis, F. D. Fuller, and J. P. Ogilvie, *Opt. Express* **18**, 11015 (2010).
- [12] J. Yuen-Zhou, J. J. Krich, and A. Aspuru-Guzik, *The Journal of Chemical Physics* **136**, 234501 (2012).
- [13] H. Li, A. P. Spencer, A. Kortyna, G. Moody, D. M. Jonas, and S. T. Cundiff, *J. Phys. Chem. A* **117**, 6279 (2013).
- [14] J. A. Cina, P. A. Kovac, C. C. Jumper, J. C. Dean, and G. D. Scholes, *The Journal of Chemical Physics* **144**, 175102 (2016).
- [15] T. N. Do, M. F. Gelin, and H.-S. Tan, *The Journal of Chemical Physics* **147**, 144103 (2017).
- [16] V. Perlik, J. Hauer, and F. Šanda, *J. Opt. Soc. Am. B* **34**, 430 (2017).
- [17] C. L. Smallwood, T. M. Autry, and S. T. Cundiff, *J. Opt. Soc. Am. B* **34**, 419 (2017).
- [18] V. Engel, *Computer Physics Communications* **63**, 228 (1991).
- [19] M. F. Gelin, D. Egorova, and W. Domcke, *The Journal of Chemical Physics* **123**, 164112 (2005).
- [20] M. F. Gelin, D. Egorova, and W. Domcke, *The Journal of Chemical Physics* **131**, 194103 (2009).
- [21] K. Renziehausen, P. Marquetand, and V. Engel, *Journal of Physics B: Atomic, Molecular and Optical Physics* **42**, 195402 (2009).
- [22] J. Yuen-Zhou, J. J. Krich, I. Kassal, A. S. Johnson, and A. Aspuru-Guzik, *Ultrafast Spectroscopy* (IOP Publishing, 2014).
- [23] P. A. Rose and J. J. Krich, *The Journal of Chemical Physics* **150**, 214105 (2019).
- [24] P. A. Rose and J. J. Krich, "Automatic Feynman diagram generation for nonlinear optical spectroscopies," Submitted to *J Chem Phys*.
- [25] S. Mukamel, *Principles of Nonlinear Optical Spectroscopy* (Oxford University Press, 1999).
- [26] M. Beck, A. Jackle, G. Worth, and H.-D. Meyer, *Physics Reports* **324**, 1 (2000).
- [27] D. V. Tsvilin, H.-D. Meyer, and V. May, *The Journal of Chemical Physics* **124**, 134907 (2006).
- [28] J. Johansson, P. Nation, and F. Nori, *Computer Physics Communications* **183**, 1760 (2012).
- [29] J. H. Fetherolf and T. C. Berkelbach, *The Journal of Chemical Physics* **147**, 244109 (2017).
- [30] Y.-a. Yan, *Chinese Journal of Chemical Physics* **30**, 277 (2017).
- [31] A. Raab and H.-D. Meyer, *The Journal of Chemical Physics* **112**, 10718 (2000).
- [32] G. Katz, R. Kosloff, and M. A. Ratner, *Israel Journal of Chemistry* **44**, 53 (2004).
- [33] F. Caycedo-Soler, A. W. Chin, J. Almeida, S. F. Huelga, and M. B. Plenio, *The Journal of Chemical Physics* **136**, 155102 (2012).
- [34] N. Killoran, S. F. Huelga, and M. B. Plenio, *The Journal of Chemical Physics* **143**, 155102 (2015).
- [35] C. Gardiner and P. Zoller, *Quantum Noise: A Handbook of Markovian and Non-Markovian Quantum Stochastic Methods with Applications to Quantum Optics (Springer Series in Synergetics)* (Springer, 2004).